Theoretical and Applied Fracture Mechanics 128 (2023) 104140

Contents lists available at ScienceDirect

Theoretical and Applied Fracture Mechanics

journal homepage: www.elsevier.com/locate/tafmec

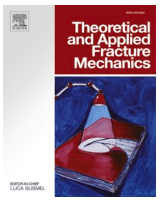

# Combined RVE-Cohesive elements approach to the multi-scale modelling of FDM 3D-printed components

A. Corvi, L. Collini *

*University of Parma, Department of Engineering and Architecture, Parco Area delle Scienze 181/A, 32124 Parma, ITALY*

ARTICLE INFO

*Keywords:*
Fused Deposition Modelling
Multi-scale modelling
Damage mechanism
RVE approach
Cohesive elements

ABSTRACT

Mechanical strength of 3D-printed components dramatically depends on printing process parameters. These can be usually set over a relatively wide range, in combinations that determine the microstructure morphology and the resulting mechanical behaviour. The present investigation focuses on the relationship between revealed structure and resulting mechanical properties of FDM-printed ABS specimens. The peculiar structures, examined at the meso- and microscale, are modelled by a finite-element Representative Volume Element (RVE) approach, in conjunction with cohesive elements to reproduce the sealing efficiency between fused filaments. The simulation of the tensile response up to failure falls within the 95% of confidence with experiments. Also, homogenized response of RVE determines spatial material constants useful for the effective numerical simulations of functional components, and intra- and inter-layer damage mechanisms are distinguished providing hints for the structural optimization.

## 1. Introduction

Many engineering applications have greatly benefited from the impressive advances made by Additive Manufacturing (AM) in recent years, as it paved the way to new productive capabilities in terms of design, materials, and structures. Among AM technologies, Fused Deposition Modelling (FDM), also known as Fused Filament Fabrication (FFF), is the most widely spread technology thanks to its low cost, good speed, and no need of a conditioned environment. This technique has been confined for years mostly to the rapid prototyping process, while only recently it has been employed to obtain structural and functional components, with good mechanical properties that could face the traditional manufacturing subtractive processes.

The performance of FDM-printed parts is severely influenced by the set of parameters chosen during the printing process. This aspect has been massively studied, mainly regarding the anisotropy of the final obtained component [1–2], the single effect of the main controllable parameters (raster angle, deposition pattern, layer height, printing speed) [3–5] or the search for optimal combination of parameters also considering the mutual interactions between factors [6].

Together with the use of FDM process for engineering components, it becomes necessary to investigate the behaviour of these parts both in safe and damage regimes. Some studies are available on the understanding of the failure of printed specimens by observing the fracture surface [7–8]; Corvi et al [9] proposed a directional damage model for components printed through filament deposition technique; Moetazedian et al [10] investigated the damage evolution of printed PLA from the loss of performance under cyclic loading; Aliheidari et al [11] experimentally correlated the fracture energy to the printing parameters testing double-cantilever-beam specimens.

All these works highlight that FDM-printed parts present non-homogeneous mechanical resistance: the bond formation process between deposited filaments is the key phenomenon to understand. Garzon-Hernandez et al [12] proposed a methodology to design components with custom properties starting from the effect of manufacturing settings on the sintering process ruling the bonding at the interface, and Corvi et al [13] validated a thermo-mechanical model confirming that interfaces between filaments are the weakest regions in terms of internal stresses.

In this framework, the approach of using a Reference Volume Element (RVE) seems to be a valid alternative as it confines the analysis to a unit cell only, that is, in case of repetitive structures and especially when using numerical analysis, representative of the whole material behaviour at the mesoscale [14–15]. Due to the peculiar symmetry and repetition of porosities between adjacent filaments, this method has been already used with accurate results in determining the elastic

* Corresponding author.
*E-mail address:* luca.collini@unipr.it (L. Collini).

https://doi.org/10.1016/j.tafmec.2023.104140
Received 31 May 2023; Received in revised form 28 September 2023; Accepted 12 October 2023
Available online 19 October 2023

constants of FDM-printed components, e.g. in [16–17].

Given the above, in this work the influence of the main controllable process parameters on the mechanical response of a wide series of tensile specimens printed via FDM technology is investigated. To this aim, microscope observations are considered as the starting point to understand how the morphology of different specimens is affected by the set of parameters defined during the printing process. In parallel, a multi-level finite-elements model series is developed adopting the RVE approach: a unit cell is identified from microscope images as the smallest repeatable entity, and periodic boundaries conditions are applied at its borders. In addition, cohesive finite elements are introduced to describe the mechanical behaviour of junctions between deposited filaments. This is an absolute novelty for FDM parts. Cohesive elements are a powerful tool to model interfaces, employed mainly for analysis on composites, joints and adhesives [18–19]. In this work this technique allows to define an interface between filaments with tuneable strength properties, which can reproduce subsequent fractures during loading, and fully explains the damage mechanism of layered FDM structures.

Tensile load is applied, and the deforming mechanism is studied, up to the failure strain. Indeed, the damage of the component is a primary aspect that cannot be neglected, being responsible not only for the failure of the specimen but also for its progressive degradation which depends on the stress state the part is subjected to. Damage mechanisms are accurately analysed and modelled at different length scales: compared with experimental tests, simulations reveal a very good predictive capacity, allowing to state that this methodology is desirable to get more reliable and precise numerical models for additively manufactured components.

## 2. Materials & methods

### 2.1. Specimens and experimental campaign

For the purpose of the study, 35 tensile specimens with 1BA geometry according to the standard EN ISO 527–2 (5x2 mm of cross-section) are 3D-printed on a BQ Hephestos-2 printer, using the Acrylonitrile-Butadiene-Styrene (ABS) commercial filament by FormFutura®. The filament has been firstly mechanically tested to accurately compute its elastic modulus and failure strain.

The combinations of explored printing parameters are summarized in Table 1, and a qualitative scheme of resulting layered structures is shown in Fig. 1. Essentially, the parameters examined are the layer height and the raster orientation angle, in combination with three extrusion temperatures: each parameter is explored in the average and limit values of its range. N specimens are fabricated and tested for each scenario, allowing to statistically evaluate the dispersion of the responses within each family.

**Table 1**
Considered sets of process parameters.

| Scenario | N | Layer height [mm] | Printing temperature [°C] | Raster orientation |
|---|---|---|---|---|
| 1 | 5 | 0.4 | 250 | 0° |
| 2 | 5 | 0.4 | 250 | −45°/+45° |
| 3 | 5 | 0.2 | 250 | 0° |
| 4 | 5 | 0.4 | 230 | 0° |
| 5 | 5 | 0.4 | 270 | 0° |
| 6 | 5 | 0.4 | 230 | −45°/+45° |
| 7 | 5 | 0.4 | 270 | −45°/+45° |

Specimens are printed without walls (circumferential layers) not to affect the influence of the raster angle on their tensile response.

All the samples are mechanically tested in displacement control at constant rate of 3 mm/min on the uniaxial tensile Test® GMBH Universal Testing Machine - Model 112 equipped with a 2kN cell load, and data are elaborated in terms of nominal stress–strain curves, not showing the specimens any significant necking during the traction.

Specimens are cut with a razor blade mounted on a stiff support and their cross-sections observed at the microscope, capturing the layered structure morphology that generates a set of 3D CAD models. Being the microstructure almost independent from the observation area, it is possible to consider the whole part as the periodic face-to-face tessellation of a unit cell in 3D space, hence allowing the RVE approach to represent the whole material system, with the advantages shown below.

### 2.2. RVE definition and homogenization technique

Fig. 2 shows the RVE definition based on the superposition of a sample cell to a micrograph of the cross-sectional morphology.

The nearly perfect symmetry promotes the geometrical repetition of the unit cell. The layer height is the parameter that affects the RVE geometry the most. Two different values are here considered, 0.4 mm and 0.2 mm, while the deposition width is kept constant to 0.4 mm. Regarding the −45/+45° raster angle condition, the repeating unit evidenced in the cross-section observation is double size the unit found for 0° raster angle condition: the porosities between adjacent filaments are indeed oriented as the rasters themselves, meaning the porosities of two consecutive layers are extending normally to each other, see Fig. 2c. However, being the loading direction at 45° with reference to the faces of the identified unit cell, it is possible to model only a half of that, as the mechanical behavior is symmetrical between top and bottom parts.

Again, microscope observations on scenarios characterized by different values of extrusion temperature highlight that this last has a significant effect on the quality of the bonding between adjacent filaments. Fig. 3 investigates this phenomenon: higher extrusion temperature leads to a better bonding between filaments as the material viscosity is lower when deposited; on the other hand, opposite effect is noticed for values at the bottom of the temperature range, as already evidenced in [20].

The RVE method requires a proper setting of Periodic Boundary Conditions (PBCs), representative of the spatial tessellation of the unit cell. PBCs stipulate that opposite pairs of surfaces on the boundary of the RVE must deform identically under a given loading history, as expressed in Eq. (1):

$$\zeta^{N_a}_{(x,y)} = \zeta^{N_b}_{(x,y)} \text{ on boundary } \Omega_k \tag{1}$$

being $\zeta$ the considered model parameter (displacement in this work), $N_a$ and $N_b$ the sets of nodes kinematically linked on opposite edges of the

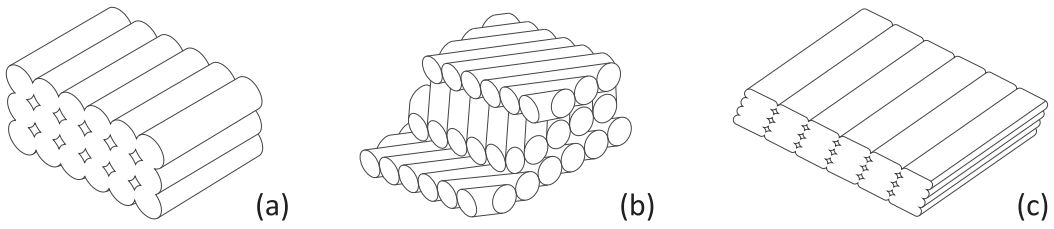


**Fig. 1.** A) 1st scenario; b) 2nd scenario; c) 3rd scenario.

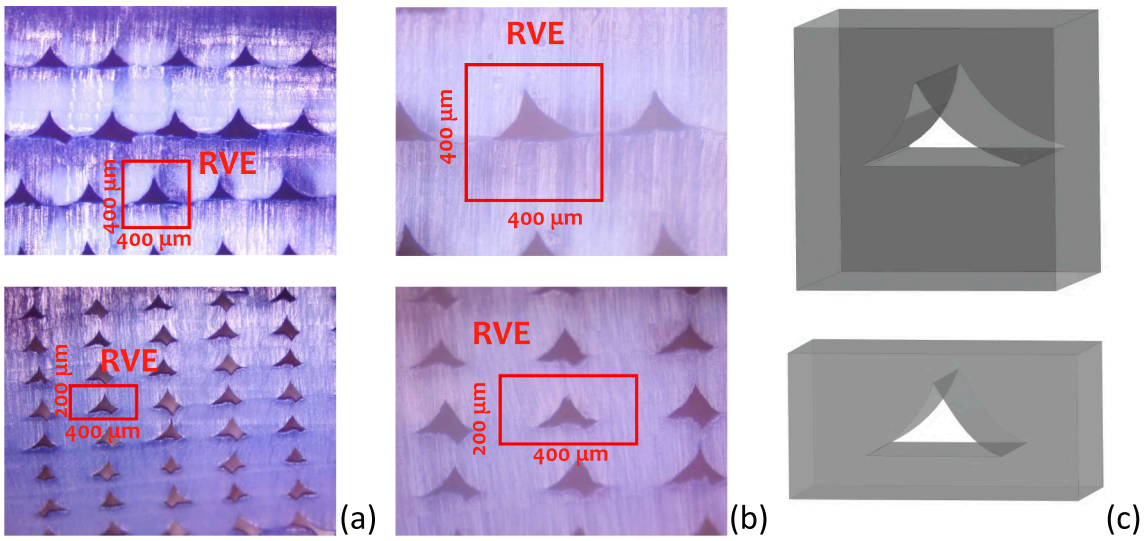


**Fig. 2.** RVE geometry from cross-sectional morphology: a) 0.4 mm layer height and 0° raster angle; b) 0.2 mm layer height and 0° raster angle; c) 0.4 mm layer height and −45/+45° raster angle.

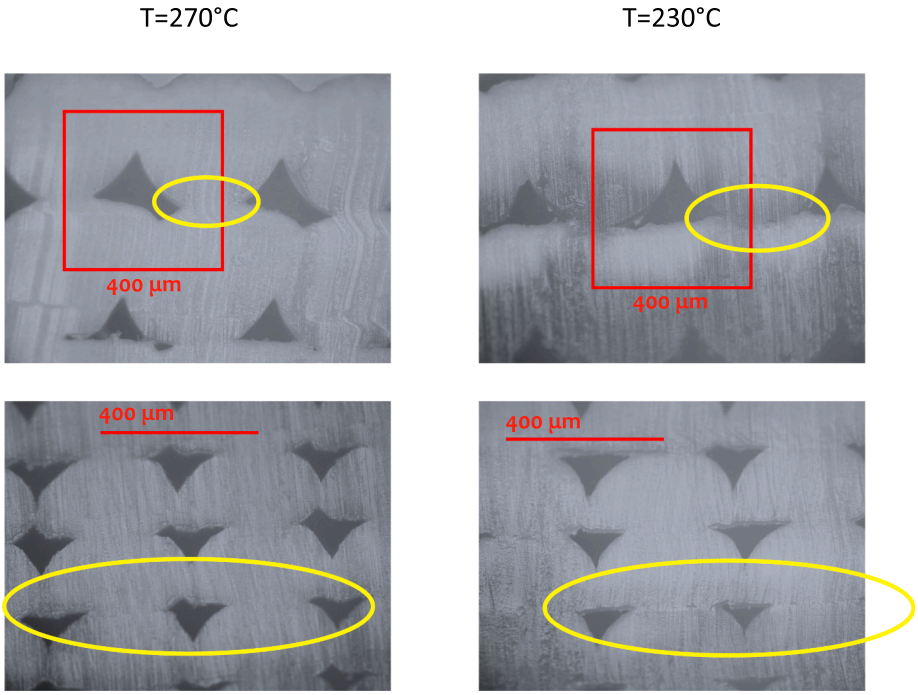


**Fig. 3.** Evidence of temperature effect on the bonding between adjacent filaments.

RVE, and *k* the top/bottom/left/right boundary of the unit cell. In the Finite-Elements (FE) code, this constraint is expressed through a set of canonical equations linking together all the degrees of freedom of nodes belonging to the boundary edge or surface, see Eq. (2):

$$A_1 {U_1}^P + A_2 {U_2}^Q + \ldots + A_N {U_k}^R = 0 \tag{2}$$

with *1, …, N* scalar coefficients and *1, …, k* the DOFs of *P, …, R* nodes. Master nodes are defined, where loads are applied, in traction or shear.

Once the RVE is defined, the classical material homogenization at a larger scale, namely the mesoscale, is followed. In this case, the ABS behaviour at the microscale is imposed and the RVE response, through loading-displacement curves and elastic constants, is obtained from the mesoscale behaviour aimed at the description of the macroscale behaviour. Indeed, the technique allows to define a homogeneous material with the same mechanical behaviour of the modelled reference volume, with no inhomogeneities, geometrical or constitutive. To do so, six independent strain fields are separately applied to the RVE, three in tension and three in shear mode, and the corresponding directional stress components developed in the RVE are extracted. Obtained numbers are the so-called "Engineering Constants" $E_1$, $E_2$, $E_3$, $G_{12}$, $G_{13}, G_{23}$ and $\nu_{12}$, $\nu_{13}, \nu_{23}$ Poisson's ratios, obtained from the compliance matrix $C^{-1}$ expressed in Eq. (3):

$$\begin{bmatrix} \bar{\varepsilon}_{11} \\ \bar{\varepsilon}_{22} \\ \bar{\varepsilon}_{33} \\ \bar{\gamma}_{12} \\ \bar{\gamma}_{13} \\ \bar{\gamma}_{23} \end{bmatrix} = \begin{bmatrix} 1/E_1 & -\nu_{21}/E_2 & -\nu_{31}/E_3 & 0 & 0 & 0 \\ -\nu_{12}/E_1 & 1/E_2 & -\nu_{32}/E_3 & 0 & 0 & 0 \\ -\nu_{13}/E_1 & -\nu_{23}/E_2 & 1/E_3 & 0 & 0 & 0 \\ 0 & 0 & 0 & 1/G_{12} & 0 & 0 \\ 0 & 0 & 0 & 0 & 1/G_{13} & 0 \\ 0 & 0 & 0 & 0 & 0 & 1/G_{23} \end{bmatrix} \begin{bmatrix} \bar{\sigma}_{11} \\ \bar{\sigma}_{22} \\ \bar{\sigma}_{33} \\ \bar{\sigma}_{12} \\ \bar{\sigma}_{13} \\ \bar{\sigma}_{23} \end{bmatrix} \tag{3}$$

The compliance matrix is the inverse of the stiffness matrix $\bar{C}$: coefficients of $\bar{C}$ are obtained performing the ratio of the volume average of corresponding stress component in RVE over the corresponding elementary strain applied in RVE, as resumed in Eq. (4):

$$\bar{C}_{ij} = \frac{\bar{\sigma}_{ij}}{\varepsilon_{ij}} \text{ where } \bar{\sigma}_{ij} = \frac{1}{V_{RVE}} \int_V \sigma_{ij} dV \tag{4}$$

Operatively, in this work the plugin Micromechanics Plugin is used in the *Dassault-Systèmes* ABAQUS© environment, due to its good flexibility in meshing, loading and periodic BCs [21].

### 2.3. Numerical modelling strategy

Two CAD models, previously shown in Fig. 2c, are imported into the numerical environment to perform FE simulations. RVE geometry is a cube with edges of 0.4 mm, except for scenario 2 in which width and height are 0.2 mm. The porosity extends for about the 7 % of the volume: geometrically, its height is about half of its length, with this last being about the 65 % of the RVE length. As for the meshing strategy, 8-node linear brick elements (C3D8) are chosen for the ABS material, justified by the unit-cell cubic geometry and by the lack of significant flexural fields, and 8-node three-dimensional cohesive elements (COH3D8) are adopted to mesh interface regions. The thickness of the cohesive zone is 10 μm and it is meshed with sweep technique and direction normal to the interface surface. The choice of not opting for a zero-thickness cohesive layer, very often used for this kind of fracture simulations, is simply due to the need of having non-coincident nodes when applying PBCs. The resulting mesh is presented in Fig. 4 for clarification.

ABS is numerically modelled through the Ramberg-Osgood constitutive law available in ABAQUS© environment in the form of Eq. (5), to appreciate a gradual transition between the elastic and the plastic behaviour, according to what is noticed from experimental tests:

$$E\varepsilon = \sigma \left[ 1 + \alpha \left( \frac{|\sigma|}{\sigma_0} \right)^{n-1} \right] \tag{5}$$

Parameters $E$, $\alpha$, $\sigma_0$ and $n$ are determined fitting at best the tensile curve of ABS filament. The damage is modelled via the ABAQUS© isotropic *Ductile Damage Model* [22], setting a damage strain value that could fit the experimental tests. A damage evolution law is also determined to describe the evolutive part, choosing a quadratic form in accordance with the behaviour experimentally noticed. The computed damage variable $d$ affects the elastic modulus $E_d$ as stated in the continuum damage mechanics theory framework, where $E$ is the modulus of the undamaged material:

$$E_d = E(1 - d) \tag{6}$$

The use of a RVE is justified, as FDM-ed components show strongly directional properties due to the dependence from the path of deposition of filaments. Experimental observations show that the most critical section results at the interface of adjacent filaments, i.e. where the two

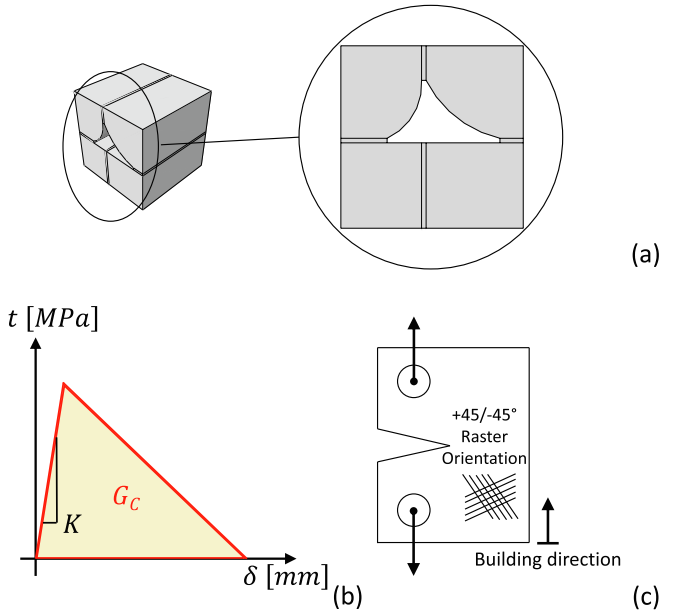


**Fig. 5.** Definition of the cohesive properties: a) Cohesive regions in RVE; b) Load-displacement response of cohesive elements; c) CT specimens for fracture toughness test.

filaments melt together, see Fig. 3. This region is typically weaker than the bulk material. Thus, interface zones, that are 4 in number for each RVE, Fig. 5a, are defined differently from the rest of the model, considering the mesoscale response which is responsible for the separation (debonding) of adjacent filaments.

Debonding and separating property is modelled by cohesive sections properly introduced in the numerical model. The elastic behaviour of the cohesive zone is expressed by Eq. (7), [23]:

$$\begin{bmatrix} t_N \\ t_S \\ t_T \end{bmatrix} = \begin{bmatrix} K_{NN} & 0 & 0 \\ 0 & K_{SS} & 0 \\ 0 & 0 & K_{TT} \end{bmatrix} \begin{bmatrix} \delta_N \\ \delta_S \\ \delta_T \end{bmatrix} \tag{7}$$

with $t_N$, $t_S$, $t_T$ being respectively the normal stress, shear stress and tear stress, and $\delta_N$, $\delta_S$, $\delta_T$ the separation, shear, and tear displacement. Here, $K$ represents the initial stiffness of the interface: as in traditional modelling of adhesive joints, the value of stiffness is significantly high as it is defined as the ratio of the elastic modulus over the adhesive thickness, that is nearly zero in this case; a value of $10^6$ MPa is frequently employed when modelling composites [23], and the same holds for this work.

The damage initiation displacement $\delta^0$ and the final separation displacement $\delta^F$, which corresponds to the complete debonding, are consequently defined as follows:

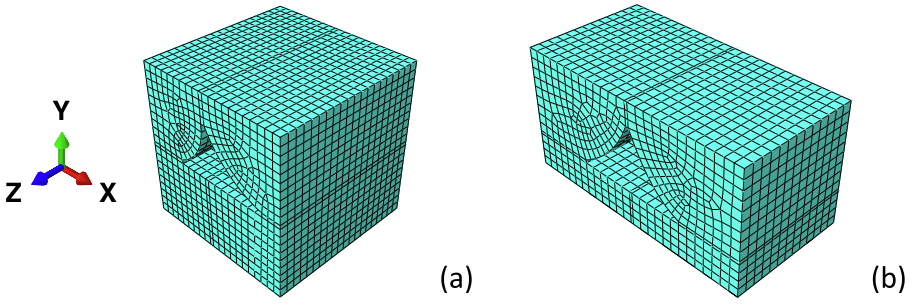


**Fig. 4.** Mesh strategy for the RVE: a) RVE for Scenario 1; b) RVE for Scenario 3.

$$\delta_N{}^0 = \frac{t_N{}^0}{K_{NN}} \qquad \delta_S{}^0 = \frac{t_S{}^0}{K_{SS}} \qquad \delta_T{}^0 = \frac{t_T{}^0}{K_{TT}} \tag{8}$$

$$\delta_N{}^F = \frac{2G_{IC}}{t_N{}^0} \qquad \delta_S{}^F = \frac{2G_{IIC}}{t_S{}^0} \qquad \delta_T{}^F = \frac{2G_{IIIC}}{t_T{}^0} \tag{9}$$

where $G_{IC}$, $G_{IIC}$, $G_{IIIC}$ are the critical fracture energies for Mode I, Mode II and Mode III, respectively, and they are responsible of the slope of the softening region in Fig. 5b.

Damage initiation threshold is defined via the maximum nominal stress criterion [24]:

$$\max\left\{\frac{\langle t_N\rangle}{t_N{}^0}; \frac{t_S}{t_S{}^0}; \frac{t_T}{t_T{}^0}\right\} = 1 \tag{10}$$

Once the condition for damage initiation is reached, the cohesive damage variable $D_c$ is computed according to Eq. (11), where $\delta_m = \sqrt{\delta_N{}^2 + \delta_S{}^2 + \delta_T{}^2}$ is the effective relative displacement in case of mixed-mode scenarios:

$$D_c = \frac{\delta_m{}^F(\delta_m - \delta_m{}^0)}{\delta_m(\delta_m{}^F - \delta_m{}^0)} \tag{11}$$

The damage variable $D_c$ affects the properties of the cohesive region, operating on $\bar{t}$ which represents the stress components predicted by the elastic traction-separation behavior for the current strains without damage. Indeed:

$$\begin{aligned} t_N &= \begin{cases} (1-D_c)\bar{t_N} & \bar{t_N} \geq 0 \\ \bar{t_N} & \bar{t_N} < 0 \end{cases} \\ t_S &= (1-D_c)\bar{t_S} \\ t_T &= (1-D_c)\bar{t_T} \end{aligned} \tag{12}$$

In this way, the RVE damage is due to two contributions: the isotropic damage of filaments, and the interface decohesion between filaments; these mechanisms are acting at the microscale, and as in typical unit cell approaches, the response is evaluated at the mesoscale. Table 2 summarizes the set of parameters adopted for the development of the numerical model.

As said, the tensile properties of ABS are determined by a tensile test of a single filament with nominal diameter of 1.75 mm and strain rate of 1.66e-3 $s^{-1}$, see Fig. 6. Although the heat during the extrusion may change the crystallinity of the polymer, this test aims at the definition of the properties of the "bulk" filament, as the printing parameters are already considered in the model. By varying the R.-O. parameters appearing in Eq. (5), the curve is fitted at best. The ductile damage model parameters are chosen from the same test, while the fracture energy $G_C$ found in [4] for CT specimens (Fig. 5c) is adopted as reference, since material, deposition path and filament diameter are the same of the present investigation; only, to cover the full nozzle temperature range here considered, i.e. 230–270 °C, a variation of ± 10 % of $G_C$ every ± 20 °C is set in accordance to what found in [11]. The fracture properties of the structure are defined equal to those of the cohesive elements adopting the "weakest-link approach", according to [4] where the direction of crack propagation is evidenced being along the interface between filaments.

Finally, the damage initiation stresses for Mode I condition are determined from the tensile curves at raster angle ± 45°, considering the influence of temperature: details are indicated in the next section 3.3. Values for Mode II/III conditions are calibrated from Mode I values according to [25–26], assuming the damage initiation stress to be proportional to the fracture load.

The last remark regards the load application to the RVEs. While the application of a traction is straightforward when filaments and loading

**Table 2**
Material parameters in the numerical model.

| | | | | |
|---|---|---|---|---|
| **ABS filament** | | | | |
| Elastic modulus $E$ [*MPa*] | 1310 | | | |
| Poisson coefficient $\nu$ [-] | 0.3 | | | |
| Plastic offset $\alpha$ [-] | 0.007 | | | |
| Yield stress $\sigma_0$ [*MPa*] | 22 | | | |
| Strain-hardening exponent $n$ [-] | 13 | | | |
| **Material ductile damage model** | | | | |
| Fracture strain [%] | 0.6 at stress triaxiality 0.33 | | | |
| Displacement at failure [*mm*] | 0.0002 | | | |
| Exponential law parameter [-] | 2 | | | |
| **Cohesive section** | | | | |
| Elastic stiffness [$MPa/mm$] | $10^6$ | | | |
| Fracture energy [$kJ/m^2$] $G_C = K_{IC}{}^2(1-\nu^2)E^{-1}$ | T [°C] | | | |
| | 230 | 1.65 | | |
| | 250 | 1.82 | | |
| | 270 | 2.00 | | |
| Damage initiation stress [*MPa*] | T [°C] | *Mode I* | *Mode II* | *Mode III* |
| | 230 | 14 | 32 | 32 |
| | 250 | 20 | 40 | 40 |
| | 270 | 27 | 56 | 56 |

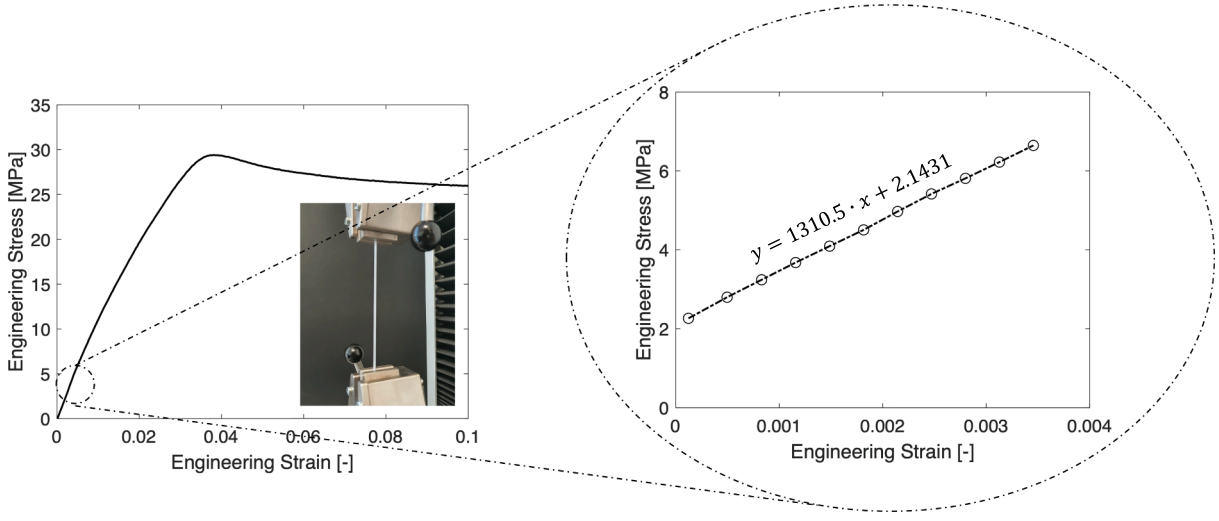


**Fig. 6.** Tensile test on a single ABS filament.

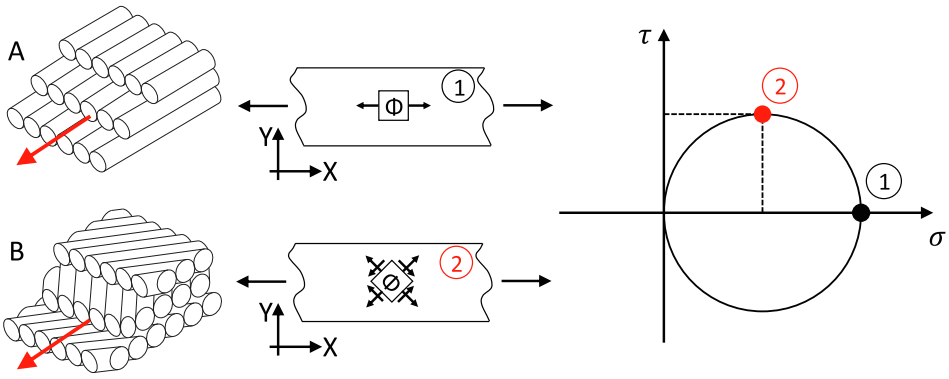


**Fig. 7.** Stress fields in scenarios 1 and 2.

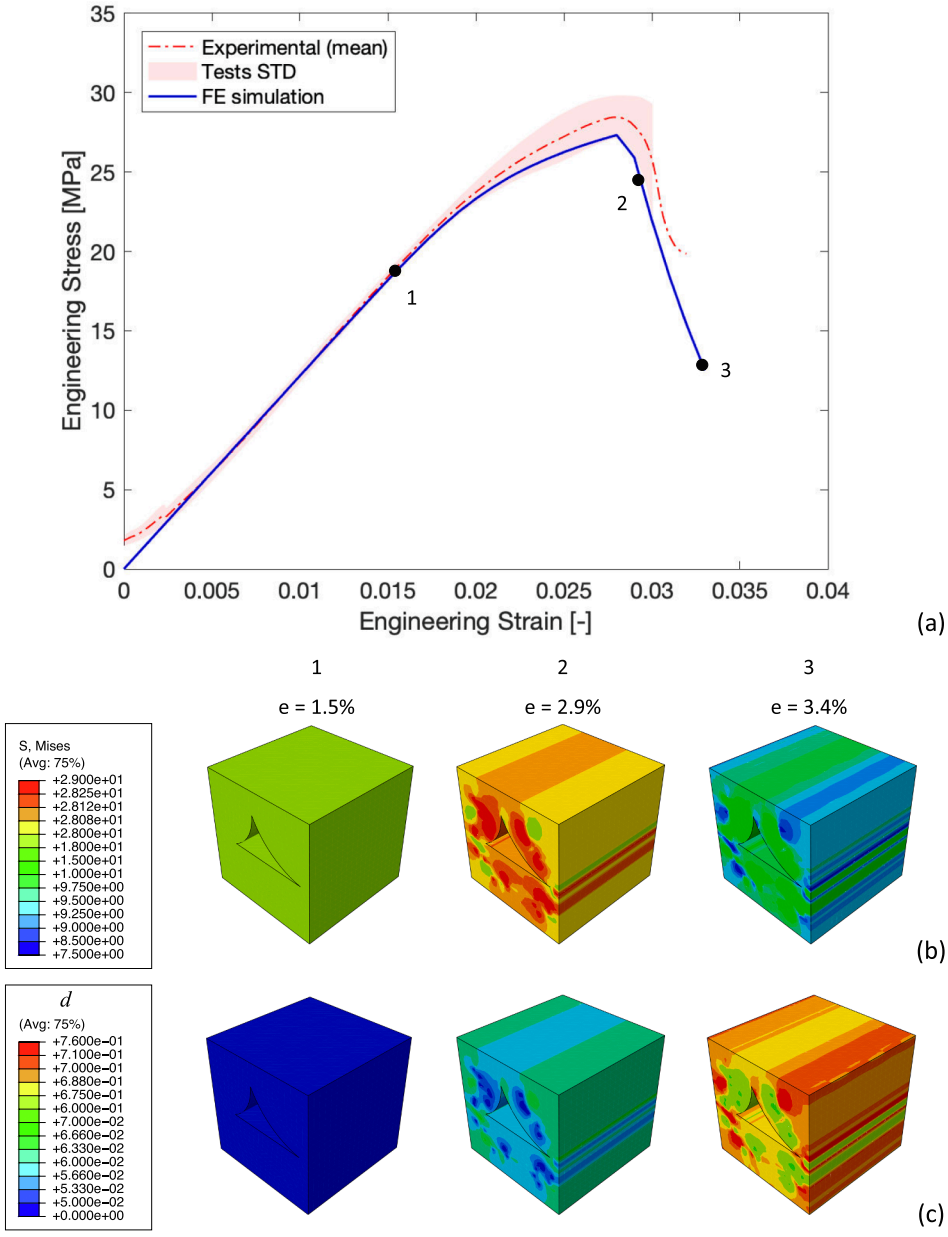


**Fig. 8.** Scenario 1: a) tensile response; b) RVE stress field at points 1, 2 and 3; c) damage evolution at the microscale.

direction are parallel, in the 45° configuration the load is applied considering an equivalent stress state: in detail, considering an infinitesimal element Φ, when the raster angle is zero the uniaxial load acts along the X-direction, situation 1 in the scheme of Fig. 7.

On the contrary, for raster angles different than zero, as the RVE is defined with 90° faces, it must be rotated by the same angle. Thus, in accordance with a Mohr's circle, a biaxial stress state along X and Y axes should be defined as producing the equivalent uniaxial tension along X. The equivalence is obtained by applying both normal and shear stress, as Fig. 7 graphically explains.

## 3. Results and discussion

### 3.1. Influence of the raster angle

The raster angle is the design parameter that mostly influences the mechanical properties (main effect). In Figs. 8 and 9 the averaged response and the standard deviation (STD) band for the 5 samples belonging to "scenario 1 – raster angle 0°" and "scenario 2 – raster angle ± 45°" is plotted. Engineering nominal quantities are considered. As for the bulk ABS, the response is linear elastic for most of the strain range, slightly deflects for a relatively short plastic regime, and abruptly falls when damage starts to occur till the rupture strain that is about 3.5 % and 2 % for the two sets, respectively. For comparison, the plots include the simulated curve by the RVE models, which shows the contours of stress and of the damage variable.

As said, the raster angle affects the damage mechanism that leads to failure. When the raster angle is 0°, i.e. all the filaments are oriented in the same direction of the load, the load-bearing capacity is relatively good, with an ultimate stress of about 28 MPa.

Accordingly, Fig. 8c shows how the damage initiates and evolves in correspondence of increasing levels of strain following the intrinsic microscale ductile damage imposed for the ABS polymer described by Eq. (6). For such a simple load, no interaction effects between filaments are evidenced by the FE model; in other words, the cohesive elements do not work as they are not subjected neither to traction-separation neither to shear loads. This means that the average value of 3.5 % for failure strain reflects the constitutive law of the filament material itself, whereas the porosity affects the elastic properties only.

A different interpretation could be given to the scenario 2 behaviour, in which the raster angle is ± 45° with respect to the loading direction. Compared to the zero angle, specimens undergo a premature failure of

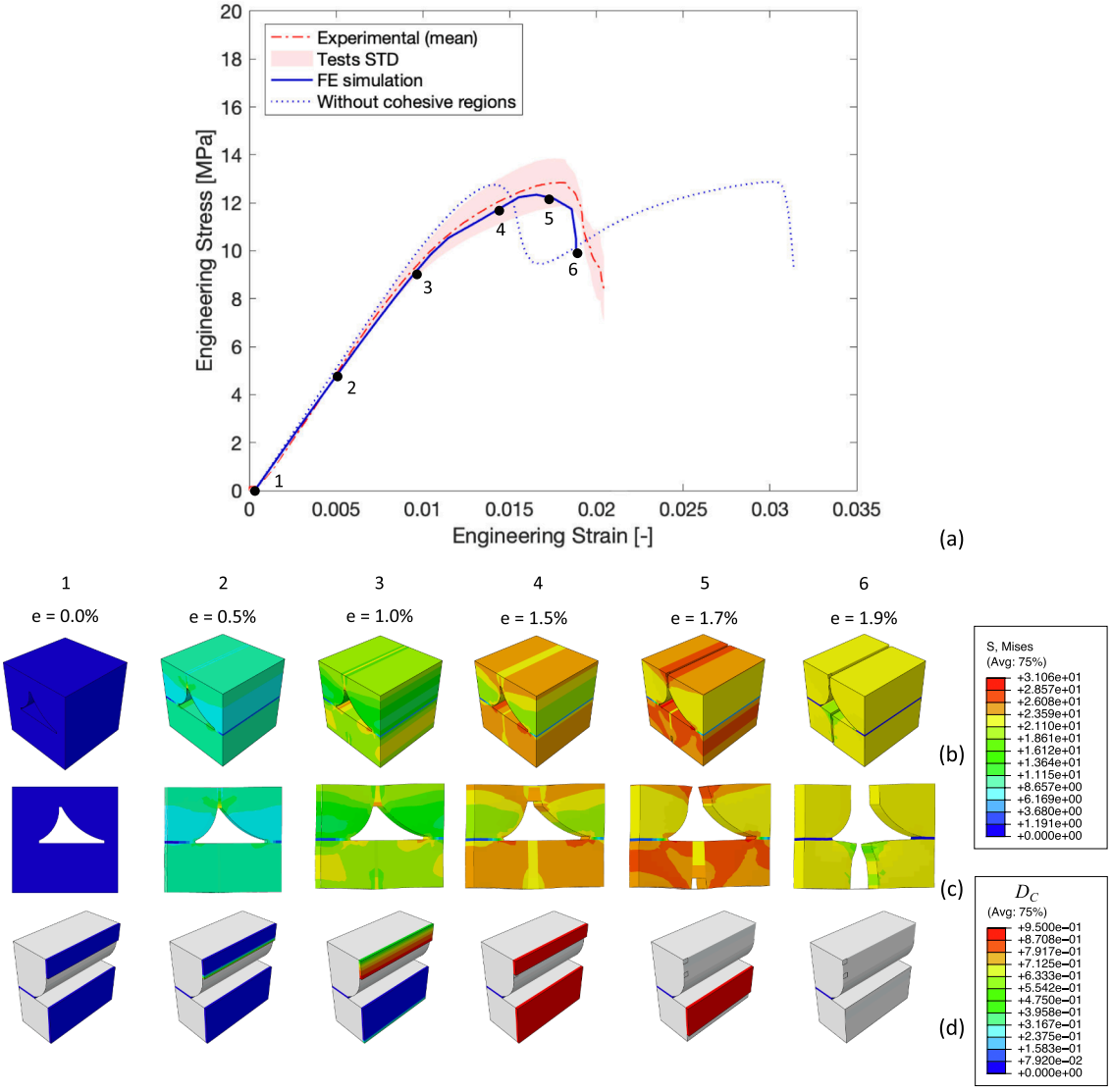


**Fig. 9.** Scenario 2: a) tensile response; b) RVE stress field at points 1, …, 6; c) detail of separation between adjacent filaments (magnitude 5x); d) damage evolution of the inter-filaments melted interface.

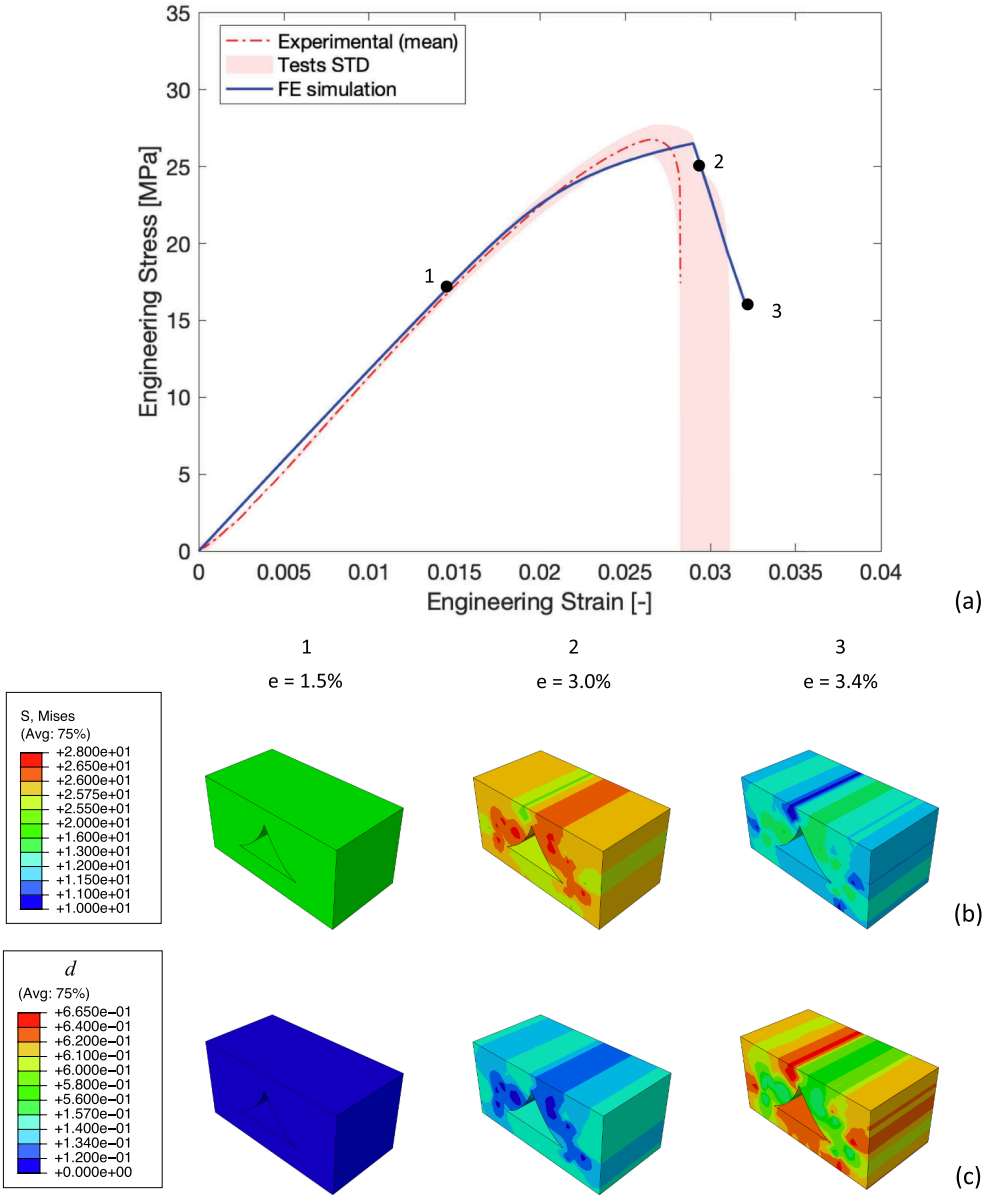


**Fig. 10.** Scenario 3: match between tests and numerical prediction.

about 50 % the failure strain, see Fig. 9.

For comparison, the same Fig. 9a illustrates with the blue dotted line the response of the RVE if no cohesive elements are modelled and activated. Here the damage mechanism does not reflect the experiments anymore, because the tensile curve drops in subsequent steps, at strain about 1.2 % and 3.2 %, corresponding to the damage of single layers one by one. In particular, the intersections between adjacent filaments, that in this model are continuous, geometrically induce local stress concentrations causing rapid stiffness degradation and load redistribution which results in a not realistic modelling approach.

Going back to the cohesive elements RVE, debonding of cohesive areas takes place between adjacent filaments formerly at the end of the elastic regime, see point 3 in Fig. 9b and 9c, hence in competition with the instauration of the ABS plastic regime. Since the RVE stress state becomes biaxial here, as previously explicated in Fig. 7, cohesive layers work in separation Mode I and shear Mode II becoming the "weakest link" firstly to undergo damage and subsequent failure. Fig. 9d illustrates the cohesive damage evolution responsible of the progressive loss in the RVE load carrying capacity, evidencing the time instants the cohesive elements start to work and then completely fail.

### 3.2. Modelling of the layer height

Here, the experimental response of specimens printed with the parameters set of Scenario 3 is compared with the FE simulation output. The match in Fig. 10 is accurate, validating the numerical model as a reliable tool to understand the influence of the layer height. Failure strain raises back to about 3 %, in accordance with the response of Scenario 1, see previous Fig. 8a, because again the damage first occurs within the filaments, and not in the weakest sealing zones between filaments. Here the filaments work essentially under uniaxial tension that acts along the same direction of deposition. This allows to state that, as one might expect, the predominant damage mechanism, or the ductility of the structure, depends on the mutual direction between load and filament deposition, i.e. on the raster angle of filament layers.

### 3.3. Influence of nozzle temperature

As previously evidenced, the temperature of the extruding nozzle significantly influences the quality of the bonding between adjacent filaments, which is consequently responsible for the strength at the

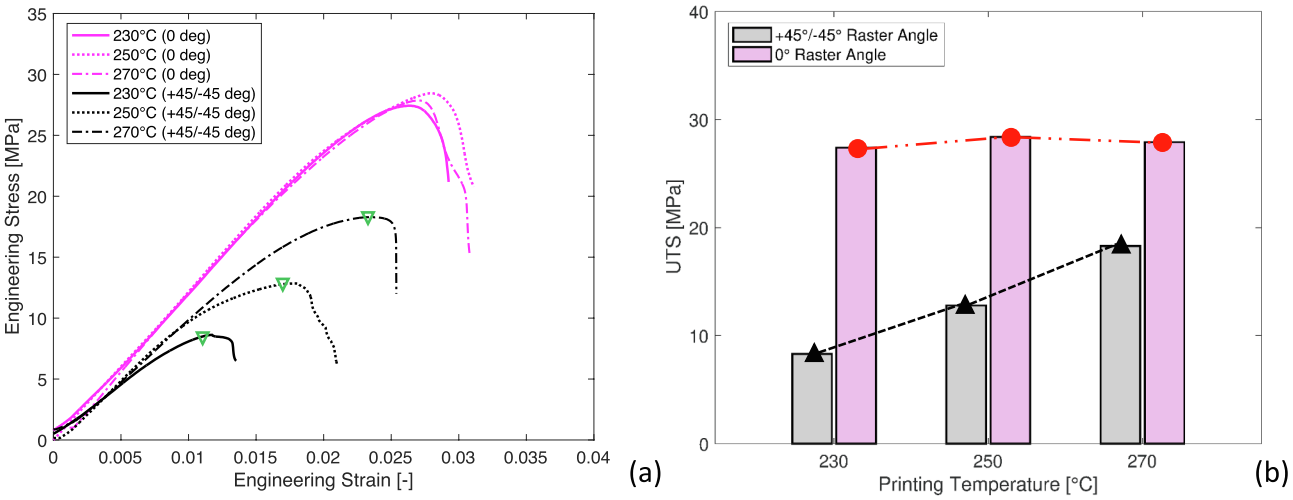


**Fig. 11.** Influence of extrusion temperature on the tensile response: a) Raster angle sensitivity; b) Trend for UTS.

interface between filaments. Looking at the tensile tests of scenarios 1–4-5 and 2–6-7, it is clear that the first family, at 0° raster angle, is not affected by the temperature value. Contrarily, the response of the second family is severely dependent from the printing temperature. Fig. 11a is aimed at evidencing this finding, being the curves at different temperature and raster angle 0° overlapping and the others well distinguishable. This fact is even clarified in Fig. 11b, which shows the ultimate tensile strength (UTS) as a function of temperature for the two families of scenarios.

These results validate what this work tries to hypothesize: specimens printed with a non-null raster angle undergo an internal stress state that is multiaxial with reference to the filament deposition orientation; consequently, the bonded interface between filaments becomes subjected to a separation load that eventually detaches the filaments and initiates micro-cracks leading to a "premature" failure.

Looking at the black curves in Fig. 11a, green markers are added in correspondence of the mesoscopic damage initiation. From these points, a set of damage initiation thresholds $t_N{}^0$, $t_S{}^0, t_T{}^0$ are determined for the cohesive elements, expressed as function of temperature. Resulting data are also anticipated in Table 2. This results with good approximation a linear form of $T$:

$$\begin{aligned} t_N^0(T)[MPa] &= 0,325T[^\circ C] - 60,92 \qquad Mode\ I \\ t_{S,T}^0(T)[MPa] &= 0,350T[^\circ C] - 48,17 \quad Mode I\ I \text{ and } III \end{aligned} \tag{13}$$

The match between simulations and experiments is now appreciable, validating the model not only as accurate in reproducing the material behaviour, but also making it a tool for predicting and optimizing the printing path once the principal stresses are known. This main result is shown in Fig. 12, where the response of the RVE is plotted against the printing temperature variation with previously determined parameters.

Looking at the green curves in Fig. 12 (270 °C), numerical outputs underestimate the maximum nominal stress reached during the tensile test, despite the elastic region being well reproduced. This discrepancy could be due to the fact that for such high temperature the extruded filament has a very low viscosity: morphology for Scenario 7 is the limit of representativity of the RVE approach as the material is all fused and so a combination of different failure mechanisms takes place.

However, the limitation for the proposed approach concerns only values above the suggested temperature range for FDM printing of commercial filaments, near the material limit for printability, allowing to state that the predictive potentiality of the modelling approach is promising.

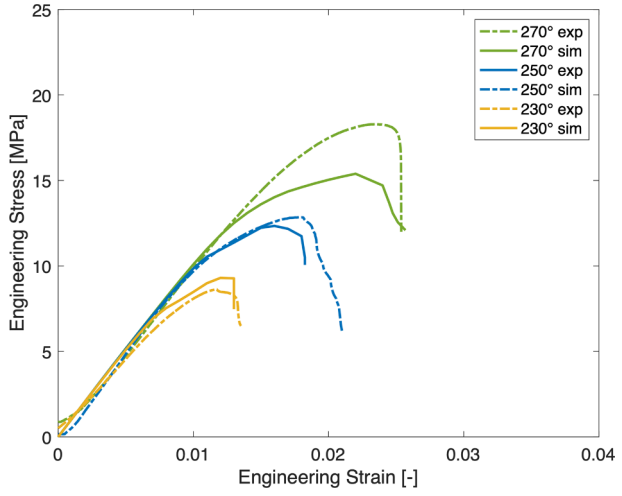


**Fig. 12.** Simulation of the extrusion temperature effect on scenarios 2,6,7.

### 3.4. Homogenization of the RVE elastic properties

As final result, the elastic properties of the RVE are obtained by homogenizing with the technique described below. Elastic constants can be assigned to a printed component as descriptive of the behaviour at the macroscale, once the local direction of printing is known, for example by adopting an anisotropic material model. When the six independent strains shown in Fig. 13 are applied to the RVE, the compliance matrix of Eq. (14) is obtained.

$$\bar{C} = \begin{bmatrix} 1221.2 & 320.98 & 462.65 & 0 & 0 & 0 \\ & 863.57 & 355.37 & 0 & 0 & 0 \\ & & 1461.9 & 0 & 0 & 0 \\ & & & 338.70 & 0 & 0 \\ & \text{symm} & & & 422.38 & 0 \\ & & & & & 462.65 \end{bmatrix} \tag{14}$$

what shown is the case of the FDM-printed ABS with 0.4 mm layer height. From that, the engineering constants of an equivalent homogenized material summarized in Table 3 can be drawn.

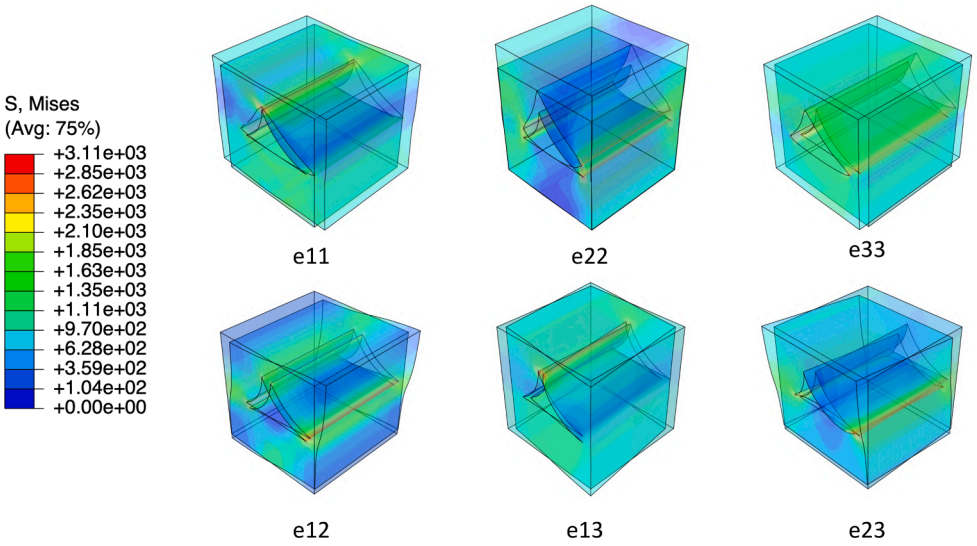


**Fig. 13.** Deformation of the RVE with six independent straining conditions.

**Table 3**
RVE engineering constants.

| $E_{11}$ [MPa] | $E_{22}$ [MPa] | $E_{33}$ [MPa] | $G_{12}$ [MPa] | $G_{13}$ [MPa] | $G_{23}$ [MPa] |
|---|---|---|---|---|---|
| 1014.5 | 736.5 | 1216.4 | 336.6 | 421.8 | 342.3 |

## 4. Conclusions

In this work, the effect of the main tuneable parameters, i.e. layer height, nozzle temperature and raster angle, on the tensile response of FDM-printed specimens is explored and modelled. Starting from microscope observations of the cross-sectional morphology, an RVE is defined, which considers the geometrical features together with a novel definition of damage initiation and evolution. More in details, plasticity is due to the filament material at the microscale, but at the mesoscale the damage onset and evolution are governed by the printing path. What triggers these two mechanisms is the stress state and the mutual orientation between principal stress and filament deposition direction. The RVE correctly predicts that ductility and strength are directly related to these mechanisms.

Other peculiar findings of this work can be summarized as follows:

- the multi-scale combined RVE-cohesive elements approach is accurate in reproducing the response of components produced via FDM technique;
- the raster angle is the predominant parameter in determining the failure, while the nozzle temperature is only responsible of an eventual premature failure; the layer height does not remarkably affect the damage mechanism nor its amount;
- homogenization reveals to be a useful technique to obtain all the components of the material stiffness matrix, allowing to accurately model macroscopic 3D-printed parts by assigning homogenized properties.

## Declaration of Competing Interest

The authors declare that they have no known competing financial interests or personal relationships that could have appeared to influence the work reported in this paper.

## Data availability

Data will be made available on request.

## Acknowledgments

Project funded under the National Recovery and Resilience Plan (NRRP), Mission 4 Component 2 Investment 1.5 - Call for tender No. 3277 of 30/12/2021 of Italian Ministry of University and Research funded by the European Union – NextGenerationEU Award Number: Project code ECS00000033, Concession Decree No. 1052 of 23/06/2022 adopted by the Italian Ministry of, CUP D93C22000460001, "Ecosystem for Sustainable Transition in Emilia-Romagna" (Ecosister).

## References

[1] C.S. Lee, et al., Measurement of anisotropic compressive strength of rapid prototyping parts, J. Mater. Process. Technol. 187–188 (2007) 627–630.
[2] N. Zohdi, R.C. Yang, Material anisotropy in additively manufactured polymers and polymer composites: A Review, Polymers 13 (2021) 3368.
[3] W. Wu, et al., Influence of layer thickness and raster angle on the mechanical properties of 3D-Printed PEEK and a comparative mechanical study between PEEK and ABS, Materials 8 (2015) 5834–5846.
[4] T.D. McLouth, et al., The impact of print orientation and raster pattern on fracture toughness in additively manufactured ABS, Addit. Manuf. 18 (2017) 103–109.
[5] J.T. Cantrell, et al., Experimental characterization of the mechanical properties of 3D-printed ABS and polycarbonate parts, Rapid Prototyp. J. 23 (4) (2017) 811–824.
[6] H. Zakaria, et al., Optimization of process parameters in fused filament fabrication (FFF) utilizing poly lactic acid (PLA), IOP Conference Series: Materials Sci. and Eng. 670 (2019) 012060.
[7] M.R. Khosravani, et al., Fracture behavior of additively manufactured components: A review, Theor. Appl. Fract. Mech. 109 (2020) 102763.
[8] S. Sharafi, et al., A review of factors that influence the fracture toughness of extrusion-based additively manufactured polymer and polymer composites, Addit. Manuf. 38 (2021) 101830.
[9] A. Corvi, et al., Analysis and modelling of damage mechanism in FDM 3D-printed lattice structure under compression loading, J. Mech. Sci. Technol. 37 (3) (2023) 1089–1095.
[10] A. Moetazedian, et al., Damage in extrusion additive manufactured biomedical polymer: Effects of testing direction and environment during cyclic loading, J. Mech. Behav. Biomed. Mater. 118 (2021) 104397.
[11] N. Aliheidari, et al., Interlayer adhesion and fracture resistance of polymers printed through melt extrusion additive manufacturing process, Mater. Des. 156 (2018) 351–361.
[12] S. Garzon-Hernandez, et al., Design of FDM 3D-printed polymers: an experimental-modelling methodology for the prediction of mechanical properties, Mater. Des. 188 (2020) 108414.
[13] A. Corvi, et al., Influence of process parameters on temperature field and residual strain in FFF-printed parts, J. Mech. Sci. Technol. 37 (11) (2023) *in press*.
[14] L. Collini, A. Pirondi, Microstructural, multilevel simulation of notch effect in ferritic ductile cast iron under low cycle fatigue, Int. J. Fatigue 162 (2022) 106993.
[15] G. Nicoletto, et al., Analysis of nodular cast iron microstructures for micromechanical model development, Strain 42 (2) (2006) 89–96.
[16] M.S. Anoop, P. Senthil, Homogenisation of elastic properties in FDM components using microscale RVE numerical analysis, J. the Brazilian Society of Mechanical Sc, and Eng. 41 (2019) 540.

[17] P. Ferretti, et al., Representative volume element (RVE) analysis for mechanical characterization of fused deposition modeled components, Polymers 13 (2021) 3555.
[18] S.R. Hallett, P.W. Harper, Modelling delamination with cohesive interface elements, 2- Numerical modelling of failure in advanced composite materials, Woodhead Publishing Series in Composites Sci. and Eng. (2015) 55–72.
[19] A. Mubashar, et al., Modelling damage and failure in adhesive joints using a combined XFEM-cohesive element methodology, J. Adhes. 90 (2014) 682–697.
[20] A.R. Zekavat, et al., Investigating the effect of fabrication temperature on mechanical properties of fused deposition modeling parts using X-ray computed tomography, Int. J. Adv. Manuf. Technol. 100 (2019) 287–296.
[21] *Micromechanics Plugin for Abaqus/CAE,* version 1.18 2022.
[22] *Abaqus User's Manual,* Dassault Systemes, v. 2022.
[23] G.R. Ibrahim, A. Albarbar, A new approach to the cohesive zone model that includes thermal effects, Compos. B Eng. 167 (2019) 370–376.
[24] R. Rafiee, S. Sotoudeh, A cohesive zone model for predicting the initiation of Mode II delamination in composites under cyclic loading, J. Reinf. Plast. Compos. 40 (5–6) (2021) 179–192.
[25] B. Ameria, et al., Fracture loads prediction of the modified 3D-printed ABS specimens under mixed-mode I/II loading, Eng. Fract. Mech. 235 (2020) 107181.
[26] N. Razavi, et al., Mixed-mode fracture prediction of acrylonitrile butadiene styrene fabricated via fused deposition modeling, Proc IMechE Part l: J Materials: Design and Applications 237 (5) (2023) 1042–1053.